Title: Optimizing aerial imagery collection and processing parameters for drone-based individual tree mapping in structurally complex conifer forests

Authors:

Derek J. N. Young*; Department of Plant Sciences, University of California, Davis, CA 95616

Michael J. Koontz; Earth Lab, University of Colorado, Boulder, CO 80303

JonahMaria Weeks; Department of Environmental Science and Policy, University of California, Davis, CA 95616

*Corresponding author. Email address: djyoung@ucdavis.edu

Abstract

Recent advances in remotely piloted aerial systems ("drone") and imagery processing enable individual tree mapping in forests across broad areas with low-cost equipment and minimal ground-based data collection. One such method involves collecting many partially overlapping aerial photos, processing them using "structure from motion" (SfM) photogrammetry to create a digital 3D representation, and using the 3D model to detect individual trees. SfM-based forest mapping involves myriad decisions surrounding methods and parameters for imagery acquisition and processing, but it is unclear how these individual decisions or their combinations impact the quality of the resulting forest inventories.

We collected and processed drone imagery of a moderate-density, structurally complex mixed-conifer stand. We tested 22 imagery collection methods (altering flight altitude, camera pitch, and image overlap), 12 imagery processing parameterizations (image resolutions and depth map filtering intensities), and 286 tree detection methods (algorithms and their parameterizations) to create 7,568 tree maps. We compared these maps to a 3.23-ha ground-truth map of 1,916 trees > 5 m tall that we created using traditional field survey methods.

The accuracy of individual tree detection (ITD) and the resulting tree maps was generally maximized by collecting imagery at high altitude (120 m) with at least 90% image-to-image overlap, photogrammetrically processing images into a canopy height model (CHM) with a 2-fold upscaling (coarsening) step, and detecting trees from the CHM using a variable window filter after applying a moving-window mean smooth to the CHM. Using this combination of methods, we mapped trees with an accuracy exceeding expectations for structurally complex forests (for overstory trees > 10 m tall, sensitivity = 0.69 and precision = 0.90). Remotely-measured tree heights corresponded to ground-measured heights with R^2 = 0.95. Accuracy was higher for taller trees and lower for understory trees, and would likely be higher in lower density and less structurally complex stands.

Our results may guide others wishing to efficiently produce broad-extent individual-tree maps of conifer forests without investing substantial time tailoring imagery acquisition and processing parameters. The resulting tree maps create opportunities for addressing previously intractable ecological questions and informing forest management.

Introduction

Forest inventories characterize the species, size, condition, and location of individual trees and are critical resources for advancing ecological theory and informing forest management (Hubbell et al., 1999; Lasky et al., 2014; North et al., 2021; Whittaker, 1956; Wright et al., 2010; D. Young et al., 2020). Forest inventories are traditionally completed by ground-based field crews and require substantial time, labor, and financial investment, which limits their spatial extent and continuity (Gray et al., 2012; USDA Forest Service, 2016). To address these constraints, forest mapping approaches have more recently employed remote sensing data to create continuous forest inventories over broad areas. Remote sensing-based forest mapping has traditionally taken an "area-based" approach in which remote sensing data (e.g., spectral reflectance data from satellite or aerial imagery) are used to estimate forest summary statistics such as tree density, mean tree height, and aboveground biomass (De Luca et al., 2019; Jayathunga et al., 2018; Puliti et al., 2019; Rodman et al., 2019). However, the increasing quality of remote sensing data and processing workflows has recently enabled remote forest mapping more analogous to field-based approaches that involve detecting and characterizing individual trees (Jeronimo et al., 2018; Koontz et al., 2021; Swayze et al., 2021).

Small remotely piloted aerial systems (RPAS, or "drones") provide data at a scale particularly well suited for individual tree detection (ITD). A fundamental technique in drone-based forest mapping involves collecting many partially overlapping images in a dense grid over the study area (Dandois & Ellis, 2013; Westoby et al., 2012). The images are supplied to a photogrammetry algorithm, which employs principles of perspective and triangulation to estimate the 3D structure of the landscape by quantifying the amount by which landscape features move relative to each other between images. This method is commonly referred to as "structure from motion" (SfM; Dandois & Ellis, 2013; Westoby et al., 2012) because the many optical perspectives from the drone as it moves allows modeling of the 3D structure of objects and landscapes. The structure data can be represented as a point cloud in which each point identifies a surface (e.g., leaf, stem, ground) that appears in multiple photos. The point cloud data can be processed into raster-format vegetation canopy height models (CHMs) (Fig. 1). SfM-derived point cloud data share many characteristics with point clouds derived from aerial light detection and ranging (LiDAR), also known as aerial laser scanning (ALS), which can also be used for ITD (Jeronimo et al., 2018; Zaforemska et al., 2019). A major difference is that SfM-derived point clouds are usually substantially denser and higher resolution (e.g., > 100 points m^{-2}, this study) than LiDAR-derived point clouds (often < 8 points m^{-2}; USGS, 2018; Weinstein et al., 2021). Relative to SfM data, airborne LiDAR data usually have larger footprints and may better capture sub-canopy structure because some laser pulses penetrate the canopy (Jayathunga et al., 2018; Lisein et al., 2013). However, drone-based SfM data is much less costly to obtain and can be collected from specific focal areas with high frequency and minimal advance planning (Camarretta et al., 2020; Mlambo et al., 2017).

Numerous algorithms have been developed to detect individual trees from CHMs (Popescu & Wynne, 2004) and directly from point clouds (Li et al., 2012; Xiao et al., 2019). ITD accuracy varies considerably depending on the stand structural characteristics and algorithms used, with higher accuracy in lower-density stands and in overstory vs. understory trees. ITD accuracy is arguably best summarized using the F-score, which incorporates the rates of both correct and false positive detections. The F-score is calculated as the harmonic mean of the sensitivity (proportion of field trees detected) and the precision (proportion of detected trees that match field trees) and which ranges between 0 (no field trees detected) and 1 (all field trees detected and no false positive detections). Recent ITD work using drone-derived SfM products for overstory trees (Creasy et al., 2021; Mohan et al., 2017) or for all trees in low- to moderate-density stands (Belmonte et al., 2020; Bonnet et al., 2017; Swayze et al., 2021) has obtained F scores ranging roughly between 0.75 and 0.85, whereas for higher-density stands or understory trees, performance tends to be lower (e.g., F < 0.65; Creasy et al., 2021). The height and canopy extent of automatically detected trees can usually be measured from CHM or point cloud data with high accuracy (RMSE: 3-7% and R^2 > 0.70; Belmonte et al., 2020; Creasy et al., 2021; Silva et al., 2016), though the narrow tops of standing dead trees can be missing in the 3D reconstruction, leading to underestimates of dead tree height (Koontz et al., 2021).

Despite the promise of drone-based tree mapping using SfM, relatively little work has quantitatively evaluated the influence of different imagery collection, imagery processing, and tree detection methods on the accuracy of the resulting tree maps. Using an oblique (as opposed to directly downward, or “nadir”) camera pitch can increase the accuracy of digital terrain models derived from drone images in areas with low vegetation cover (Nesbit & Hugenholtz, 2019) and in forests can increase the point cloud density in the understory (Díaz et al., 2020). However, the only published evaluation of camera pitch specifically in the context of individual tree detection (ITD) found that tree detection accuracy was greater with a nadir vs. oblique camera pitch (Swayze et al., 2021). Flight (image collection) altitude may additionally affect 3D reconstruction quality likely through its effect on the spatial resolution of the resulting imagery (higher altitude results in coarser grain imagery) (Dandois et al., 2015). Though previous work has found little difference in ITD performance among flights conducted between 64 and 115 m above ground level (Swayze et al., 2021) and between 50 and 100 m above ground level (Torres-Sánchez et al., 2018). Finally, while increased image collection density (i.e., overlap) is associated with increased point cloud quality and density (Dandois & Ellis, 2013; Frey et al., 2018; Ni et al., 2018), it also increases image dataset size and acquisition and processing times. Increasing image overlap can increase ITD accuracy (Swayze et al., 2021), but provides diminishing returns to accuracy at increasingly high overlap (Torres-Sánchez et al., 2018).

Image resolution and outlier filtering are key parameters that can be adjusted during the SfM processing. A strong understanding of photogrammetric analysis principles can provide key insights into how these parameters may be adjusted to yield more successful 3D reconstructions (Over et al., 2021; USGS, 2017), but empirical validation of these workflows in the context of forest inventories is generally lacking. Only one study to our knowledge has evaluated image resolution and point cloud filtering parameters in the context of ITD (Tinkham & Swayze, 2021). Using the Metashape v1.6.4 photogrammetry software (Agisoft, LLC), Tinkham & Swayze (2021) found that retaining maximal image resolution and minimizing outlier filtering during point cloud generation yielded the greatest ITD performance. However, this study did not evaluate the influence of image resolution during the alignment stage. Using full image resolution during processing may increase point cloud detail and density (Jayathunga et al., 2018; Lisein et al., 2013), but (a) higher resolution data can substantially increase processing times, (b) high-resolution images may be difficult to align and compare when they include small surfaces like leaves and branches that move or blow in the wind, and (c) the extent to which any increase in point cloud detail translates to improved ITD performance is not well known.

Finally, once photogrammetric products are generated, there are myriad options for ITD algorithm selection and parameterization. Several studies have compared the accuracy of different ITD algorithms and/or parameterizations applied to SfM-derived canopy height models and point clouds. Mohan et al. (2017) tested 4 different parameterizations of a CHM-based fixed window filter, combined factorially with 4 different CHM smoothing intensities, for a total of 16 parameter sets. Creasy et al. (2021) evaluated 97 different parameterizations of a CHM-based variable- and fixed- window filtering method (Plowright, 2021). Shin et al. (2018) tested 16 parameterizations of a point cloud-based ITD algorithm (Li et al., 2012). Koontz et al. (2021) tested a total of 177 parameter sets across 7 different CHM- and point cloud-based ITD algorithms, identifying a parameterization of a point cloud-based method (Roussel, 2021b) as the most accurate. While it also included a test of a variable window filtering algorithm (Plowright, 2021), it tested only 3 parameter sets for this algorithm based on previous results from LiDAR acquisitions (Popescu and Wynne, 2004) and thus provides limited opportunity for comparison with previous studies that employed this method.

While work to date has quantified the influence of flight and photogrammetry parameters on the resulting photogrammetry products, few studies have evaluated how these parameters affect the accuracy of the forest inventory--the ultimate product that informs ecological inference and management decisions. Further, evaluations of SfM-based tree detection algorithms to date have generally not simultaneously considered the role of imagery collection and processing parameters that create the photogrammetry products. Evaluating the influence of these categories of variables jointly may allow detection of consistent effects vs. idiosyncrasies and may reveal important interactions that enable meaningful improvements in ITD accuracy and efficiency. In addition, many evaluations of ITD methods have been conducted in stands with relatively simple structure and low tree density, potentially yielding parameter selection and tree detection performance different than may be expected in higher-density, more structurally-complex stands. In the present study, we evaluate multiple factorial combinations of imagery collection parameters (flight altitude, camera pitch, and image overlap), imagery processing parameters (image resolution for image alignment and for dense cloud generation, and point cloud outlier filtering intensity), and tree detection methods (algorithm and parameterization), for a total of 7,568 combinations, in a moderately dense, structurally complex mixed-conifer stand in the Sierra Nevada of California.

Methods

Overview

We created a ground-truth tree map of 1,916 trees > 5 m tall in a 3.23-ha focal area using traditional survey methods. We also used automated algorithms to create 7,568 alternative tree maps for this area from aerial imagery collected by drone to evaluate the influence of image acquisition and processing parameters on aerial tree mapping accuracy. In Stage 1, we identified the best-performing photogrammetry processing processing parameters and automated tree detection methods. In Stage 2, we applied those methods to identify the best image acquisition parameters (e.g., flight altitude, camera pitch, and image overlap) (Table 1).

Table 1: The combination of photo set parameters, photogrammetry parameters, and tree detection methods tested. Within each row, all factorial combinations of the listed photo set parameters, photogrammetry parameters, and tree detection methods were tested.

Comparison stage	Photo set parameters tested (Table 3)	Photogrammetry parameters tested (Table 4)	Tree detection methods tested (Appendix S2: Tables S1 and S2)	Total resulting tree maps evaluated
Stage 1 (Identify best photogrammetry and tree detection parameters)	High nadir 90/90, Low nadir 90/90	Parameter sets 7-18	VWF methods 1-228, Point cloud methods 1-58	6,864
Stage 2 (Identify best flight and image overlap parameters)	All 22 listed in Table 3	Parameter sets 9, 11, 15, 16	VWF methods 109, 110, 113, 120, 121, 122, 185, 196	704

Focal area

Our study site was a 3.23 ha mixed-conifer forest (Safford & Stevens, 2017) stand in Emerald Bay State Park on the shore of Lake Tahoe in the Sierra Nevada of California (Fig. 1a). The stand is co-dominated, in decreasing order of abundance, by ponderosa pine (*Pinus ponderosa*), incense cedar (*Calocedrus decurrens*), Jeffrey pine (*Pinus jeffreyi*), and white fir (*Abies concolor*). The stand has high structural complexity, with a continuous size distribution and small trees interspersed with larger trees and often underneath their canopies (Fig. 1b). A ground-truth stand inventory (Appendix S1, Supporting Information) revealed that the 3.23-ha focal area contained a total of 2135 trees with DBH > 7.5 cm (661 trees ha^{-1}), 1916 trees with DBH > 10 cm (593 trees ha^{-1}), 1780 trees with height > 5 m and DBH > 7.5 cm (551 trees ha^{-1}), and 1100 trees with height > 10 m and DBH > 7.5 cm (341 trees ha^{-1}). Of all trees with DBH > 7.5 cm, 292 (14%) were dead (and still standing, but potentially partially broken).

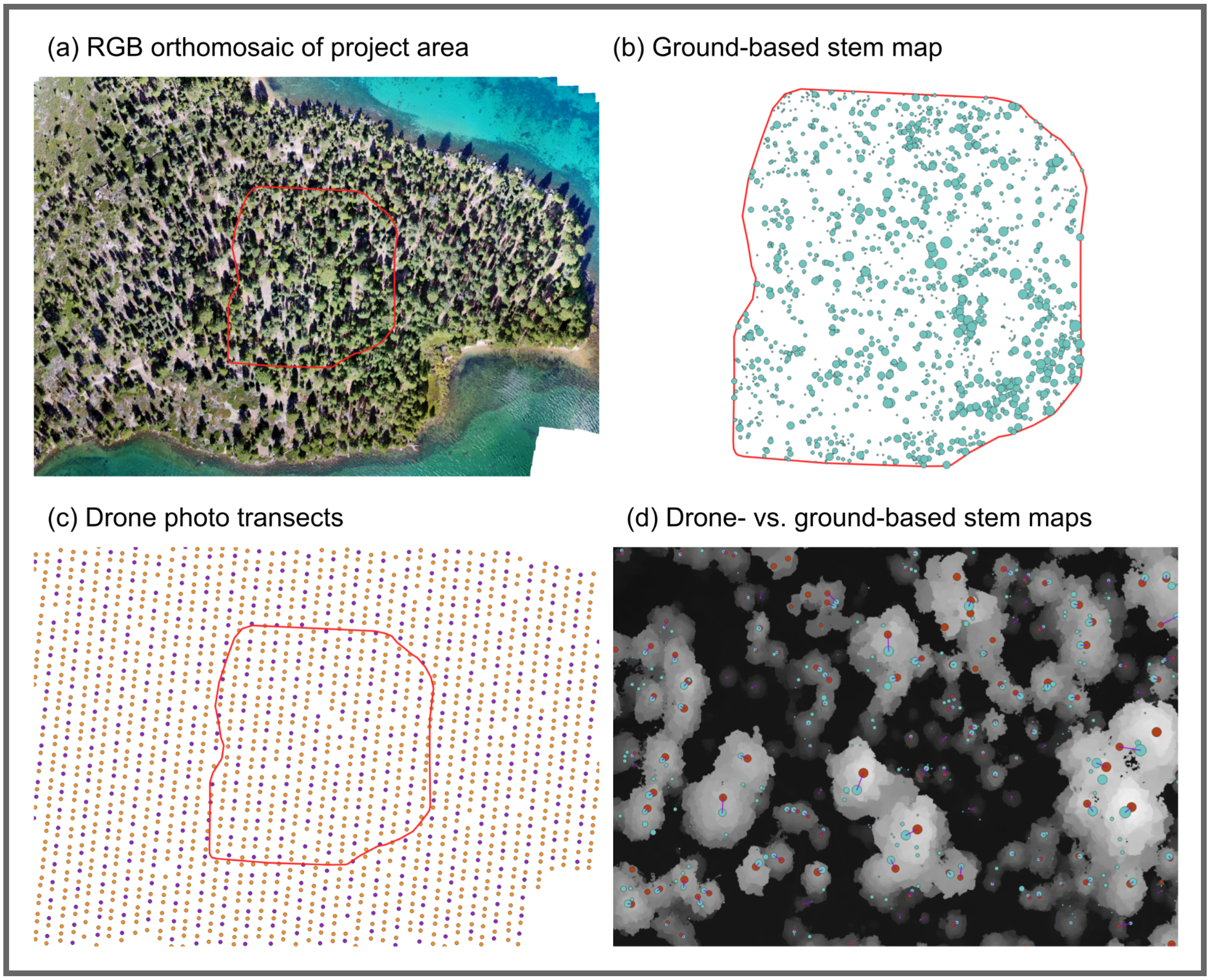

Fig. 1: (a) RGB orthomosaic of the project vicinity, with the 3.23-ha focal area indicated with a red outline. (b) The ground-based tree stem map of all trees > 5 m tall constructed as a basis for evaluation of drone-derived stem maps, with larger points indicating taller trees. (c) Spatial locations of drone photos from two drone photo sets (Table 3) ("high nadir" 95% front and side overlap in yellow; and "high nadir" 90% front and side overlap in purple). (d) Canopy height model (lighter indicates taller) of a section of the focal area, with ground-mapped trees shown as light blue points, drone-mapped trees shown as dark red points, and pairings between ground- and drone-mapped trees shown as purple lines. In (d), the canopy height model was created by applying photogrammetry parameter set 16 (Table 4) to the "high nadir" photo set with 90% front and side overlap (Table 3). The drone-derived stem map was obtained by applying tree detection algorithm "vwf_059" (Appendix S2: Table S1) to this same canopy height model.

Imagery collection and pre-processing

We collected RGB (red, green, blue) aerial photographs using a DJI Phantom 4 Advanced quadcopter (SZ DJI Technology Co., Ltd.), which has a 1", 20 megapixel (5472 x 3648 pixel) CMOS sensor, an 8.8 mm focal length, and an 84° diagonal field of view (74° horizontal field of view; 53° vertical field of view). We planned and executed missions using the

MapPilot software (Drones Made Easy) on an iPad Pro 9.3” (Apple Inc.) connected to the drone’s remote controller. The missions consisted of multiple parallel straight-line transects across the study area (and extending at least 100 m beyond it on all sides) (Fig. 1c), with transect spacing and image spacing along transects set to achieve the specified percentage of overlap between adjacent images (Table 3). Actual image overlap inevitably differs slightly from the specified overlap (e.g., due to occasionally missed photos, a normal occurrence with some common DJI drones; Fig. 1c), so we refer to the overlap amount as the “nominal overlap,” reflecting what a future user may expect when using these settings with a similar aircraft. We collected multiple image datasets using different flight parameters (altitude, gimbal pitch, and image overlap) (Table 2). For the missions with 25° camera gimbal pitch (i.e., “oblique”, with camera angled 25° up from nadir), we flew two perpendicular sets of transects (N-S and E-W) so that a given point on the landscape would be photographed from four directions. For the nadir missions, we only flew N-S transects.

All missions used automatic exposure and automatic white balance settings and were flown in MapPilot’s “connectionless” mode. We used the “terrain awareness” function so that the aircraft remained at a constant altitude above ground level (as determined by the 30m Shuttle Radar Topography Mission (Farr et al., 2007) throughout the mission. Images were collected between 11 am and 3 pm local time (where solar noon was c. 1:04 pm) on 9-12 September, 2019. During the flights, winds were light to moderate, visibility was high, and conditions were mostly clear with rare small clouds for brief periods. We used natural features, with geographic locations identified using Google Earth imagery, as ground control points (Appendix S1, Supporting Information).

To test the effect of image overlap on the quality of the resulting tree maps, we subsetted the photo sets to effectively reduce image overlap by retaining every *n*th image on every *n*th transect (Appendix S1, Supporting Information).

Table 2: Parameters for image collection flights.

Photo set (mission) name	Altitude above ground (m)	Camera gimbal pitch	Transect orientation	Forward overlap (%)	Side overlap (%)
High nadir (14)	120	0° (nadir)	N-S	95	95
Low nadir (15)	90	0° (nadir)	N-S	95	95
High oblique (26)	120	25° (oblique)	N-S	90	90
			E-W	90	90
Low oblique (27)	90	25° (oblique)	N-S	90	90
			E-W	90	90

Finally, we tested whether combining nadir (0°) and oblique (25°) camera pitch missions into a single composite photo set yielded improved photogrammetric performance and ultimately more accurate tree maps. For each flight elevation (90 m and 120 m), we prepared two composite photo sets with different overlaps (Appendix S1, Supporting Information).

Table 3: The photo set (flight and image overlap) parameters tested to evaluate the effect of flight altitude, camera pitch, and image overlap on quality of the resulting photogrammetry products for tree mapping (Stage 2). The multiple image overlap values were obtained by thinning the originally collected image datasets (Table 2). The bolded text indicates the two photo sets that were also used in identifying the best Metashape photogrammetry parameter sets (Stage 1).

Photo set group	Altitude above ground (m)	Camera gimbal pitch	Nominal image overlaps tested (front/side) (%)
High nadir	120	0°	80/80, 90/80, 80/90, **90/90**, 95/90, 90/95, 95/95
Low nadir	90	0°	80/80, 90/80, 80/90, **90/90**, 95/90, 90/95, 95/95
High oblique	120	25°	85/85, 92.5/92.5
Low oblique	90	25°	85/85, 92.5/92.5
High composite	120	0° and 25°	90/90, 95/95
Low composite	90	0° and 25°	90/90, 95/95

Photogrammetric processing and post-processing

We performed photogrammetric structure-from-motion (SfM) processing of the aerial image sets (see *Introduction*) to produce 3D point clouds and digital surface models using Metashape version 1.6.5 (Agisoft, LLC). We interfaced with Metashape via its Python API using the UC Davis Metashape workflow software version 0.1.0 (Young et al., 2021), which executes a full photogrammetry workflow from end to end using the processing parameters specified in a configuration file by the user. The workflow reads GCP location data from delimited text files prepared in advance.

Our first objective was to determine the combination of photogrammetry processing parameters that maximized the quality of the photogrammetric products for the purpose of tree mapping (Stage 1). We evaluated all factorial combinations of the photo alignment quality parameter (low, medium, or high, corresponding to image upscaling factors of 4, 2, or 1, respectively), the dense cloud quality parameter (medium or high, corresponding to image upscaling factors of 4 or 2, respectively), and the depth filtering intensity parameter (mild or moderate). Upscaling factors refer to the amount by which the image resolution was upscaled (coarsened) in each dimension; for example, with an upscaling factor of 4, the resulting image resolution in x and y dimensions would be ¼ of its original, with each coarse pixel representing the average of 16 original pixels (a 4 x 4 square) (Agisoft, 2020). Recent work has suggested the “medium” and “high” dense cloud quality parameters yield superior ITD results while avoiding extreme computational expense associated with the “very high” parameter; it has similarly shown the “mild” and “moderate” depth filtering parameters to be among those yielding best ITD performance (Tinkham & Swayze, 2021). The three-way factorial combination of photo alignment quality, dense cloud quality, and depth filtering parameters yielded 12 different processing configurations, which we ran on two different aerial photo sets: the 120 m nadir (0°

camera pitch) mission with 90% front and side photo overlap, and the 90 m nadir mission with 90% front and side photo overlap.

After identifying four Metashape parameter sets that yielded the best tree detection results for these two photo sets (see *Individual tree detection* and *Identification of best-performing methods*, below), we used each of these four parameter sets to process all of the photo sets (Table 3) to enable an evaluation of the effect of of flight altitude, image overlap, and camera pitch on tree mapping performance (Stage 2). Processing all 22 photo sets with the four Metashape parameter sets resulted in running 88 photogrammetry workflows. All processing parameters besides photo alignment quality, dense cloud quality, and depth filtering intensity were held constant across all runs (Appendix S1, Supporting Information). These included 100 maximum neighbors for dense cloud reconstruction, adaptive camera model fitting of all camera model parameters, and default Metashape Python API values for all other parameters. The workflow included a modified, automated version of a sparse point cloud filtering procedure recommended by the USGS (2017) (Appendix S1, Supporting Information). In full, the Metashape workflow had the following steps: add photos, align photos, filter sparse cloud points, add GCPs, optimize cameras (using GCPs only), filter sparse cloud points again (based on reprojection accuracy only), build dense cloud, and build digital surface model. The procedure yielded a digital surface model (DSM) and dense point cloud. The code we used to automate this workflow is published (Young et al., 2021).

We normalized and resampled the products of the photogrammetry workflow to obtain, for each run of the workflow, a CHM with 0.12 m resolution and a point cloud with 70 to 100 points m^{-2} (Appendix S1, Supporting Information).

Table 4: Metashape photogrammetry processing parameter combinations tested (Stage 1). The image upscaling factor (in parentheses) refers to the factor by which image resolution was upscaled (coarsened), in each dimension, prior to processing (photo alignment or dense cloud creation). The four parameter sets that yielded the best tree detection results and were subsequently used in the evaluations of flight altitude, camera pitch, and overlap (Stage 2) are bolded.

Photogrammetry parameter set ID	Photo alignment quality (image upscaling factor)	Dense cloud quality (image upscaling factor)	Depth filtering intensity
7	low (4)	medium (4)	mild
8	low (4)	medium (4)	moderate
9	low (4)	high (2)	mild
10	low (4)	high (2)	moderate
11	medium (2)	medium (4)	mild
12	medium (2)	medium (4)	moderate
13	medium (2)	high (2)	mild
14	medium (2)	high (2)	moderate
15	high (1)	medium (4)	mild
16	high (1)	medium (4)	moderate
17	high (1)	high (2)	mild
18	high (1)	high (2)	moderate

Individual tree detection (ITD)

During Stage 1 of methods evaluation (focused on identifying the best Metashape photogrammetry parameters and tree detection algorithms), we tested a wide range of tree detection algorithms. We first tested the “variable window filter” (VWF) algorithm of Popesu and Wynne (2004) as implemented in the R package ForestTools version 0.2.1 (Plowright, 2021). This function uses the CHM raster and evaluates each pixel as a potential tree top by searching all pixels within a particular radius around the focal pixel and labeling the focal pixel as a tree top if it has the maximum height value with the search radius. The search radius is determined by a linear function of the height of the focal pixel. We tested 76 different combinations of the intercept and slope parameters of this linear function (Appendix S2: Table S1). For each of these parameter sets, we also tested three different CHM smoothing options. These smoothing functions were implemented as moving window algorithms which, for each pixel, computed the mean of all pixels in a *n* x *n* pixel square centered around the focal pixel and assigned the resulting value to the focal pixel. We tested a 5 x 5 pixel window (Smooth: 1), a 9 x 9 pixel window (Smooth: 2), and no smooth (Smooth 0). The smooths were applied prior to running the VWF algorithm. We included these smoothing options with the thought that they may smooth over 3D reconstruction artifacts of the photogrammetry algorithm. Factorially combining the three smooth options with each of the 76 variable window filter parameter sets resulted in testing 228 implementations of the VWF-based tree detection algorithm (Appendix S2: Table S1).

We additionally tested six algorithms designed to identify trees directly from 3D point clouds, implemented in the R packages lidR v3.0.4 (Roussel, 2021a) and lidRplugins v0.2.0 (Roussel, 2021b) (Appendix S2: Table S2). Most of these algorithms accept one or more parameters; we tested a variety of parameter combinations, focusing on those that Koontz et al. (2021) found to produce the best tree detection results. Two of the algorithms ('hamraz' and 'layerstacking'; Appendix S2: Table S2) were not tested by Koontz et al. The 'hamraz' algorithm requires no parameters and 'layerstacking' requires a single binary parameter for "hardwood" or "conifer"; we tested both. Additionally, for each point cloud-based algorithm, we tested the effect of thinning ("decimating") the point cloud to 50 or 10 points m^{-2} prior to running each algorithm. The multiple parameter combinations tested across all the point cloud-based tree detection methods resulted in a total of 58 methods tested. Combined with the CHM-based VWF methods, we tested a total of 286 tree detection methods for each Metashape photogrammetry workflow that was run for the Stage 1 comparisons (Table 4). For the Stage 2 comparisons, we used four top-performing tree detection methods (see *ITD performance evaluation*).

ITD performance evaluation

We quantified the accuracy of the drone-derived tree maps by comparing each one against the 3.23-ha ground-based stem map. An initial coarse filter was applied to eliminate the very poor quality drone-derived maps: if the number of drone-mapped trees > 10 m height was more than 5 times the number of ground-mapped trees > 10 m height, or it it was less than 1/10 the number of ground-mapped trees > 10 m height, it was eliminated from the pool of candidates.

For all remaining drone-derived maps, we performed a comparison to the ground-derived map on a tree-by-tree basis, determining whether each ground-mapped tree was present in the drone-based map (true positives) and whether there were any additional trees in the drone-derived map that were not present in the ground-derived map (false positives). This required determining which tree (if any) from the ground-based map corresponded to which tree in the drone-based map (and vice-versa), a challenging and subjective exercise given that we never expect trees in a ground-based map to perfectly coincide with those in a drone-based map. Differences can arise due to spatial errors in both mapping techniques and also due to the fact that the tree top (the point identified in the drone-based map) is often not located precisely above the stem (the point identified in the ground-based map).

For a drone-mapped tree to match with a ground-mapped tree, it was required to be within a distance (d_{max}) of the ground-mapped tree defined as a function of the height (h) of the ground-mapped tree as

$$d_{max} = 0.1h + 1,$$

where units are in meters. Its height was also required to be within ±50% of the height of the ground-mapped tree. Thus, for a ground-mapped tree 10 m tall, a drone-mapped tree needed to be within 2 m distance and its height needed to be between 5 and 15 m to match. For a ground-mapped tree 30 m tall, a drone-mapped tree needed to be within 4 m distance and its height between 15 and 45 m. Our distance matching threshold was generally similar to or more conservative than that used by previous studies (e.g., < 4 m used by Swayze et al., 2021 and < 3 m used by Creasy et al., 2021). We used a more liberal height range for tree matching than previous studies (e.g., ±10% used by Creasy et al., 2021 and ±2 m used by Swayze et al., 2021) because (a) we wanted to avoid artificially reducing the estimated error in drone-based tree height measurement (as error estimation relies on comparing heights of drone-detected trees vs. paired ground-mapped trees) and (b) error substantially less than the matching threshold in drone- vs. ground-mapped height would provide evidence that trees were matched appropriately.

For each ground tree, the nearest matching drone tree was assigned as its match. If the same drone tree was assigned to multiple ground trees, it was removed from all of the ground trees except the one spatially closest to it. This procedure was repeated two more times, each time for the ground and drone trees remaining (unmatched) following the previous iteration. After the third iteration, no further matches were possible.

To quantify individual-tree detection (ITD) accuracy, we computed the true-positive rate ("sensitivity" or "recall", the proportion of ground-mapped trees that had a matching drone-mapped tree) and the precision (the proportion of drone-mapped trees that matched a ground-mapped tree). Because it is possible for a tree detection algorithm to achieve high sensitivity at the expense of precision (and vice-versa), we also computed the F score, a statistic that integrates sensitivity and precision by computing their harmonic mean, thus disproportionately penalizing low values and favoring balanced sensitivity and precision. We computed sensitivity, precision, and F score for two different tree size groups: trees ≥ 10 m height, and trees ≥ 20 m height.

There is potential for edge effects to confound the tree detection accuracy inferred via tree matching. If a ground-mapped tree were just inside the analysis boundary and the corresponding drone-mapped tree just outside it, the ground-mapped tree would be considered to not have a match (and thus constitute a false-negative detection). To minimize this effect, when calculating the proportion of drone-mapped trees that matched ground-mapped trees, we considered only drone-mapped trees that were at least 5 m inside the project boundary (so that they all had an opportunity to be matched with ground-mapped trees in any direction). We did the same with ground-mapped trees when calculating the proportion of ground-mapped trees that matched drone-mapped trees.

While it is valuable to know the proportion of all ground-truth trees that can be detected from aerial imagery, it is unrealistic to expect all trees to be detected, particularly in structurally complex stands like ours where small trees may be hidden under large trees or two immediately adjacent trees of similar size appear as one. Therefore, in addition to evaluating ITD performance across all trees, we evaluated performance in mapping "dominant" trees that did not have any immediately adjacent taller neighbors (Appendix S1, Supporting Information).

Identification of best performing methods

To identify the best performing photogrammetry and tree-detection parameter sets (Stage 1), we first determined the tree detection algorithm that yielded the greatest F score for each factorial combination of photo set (High nadir 90/90, Low nadir 90/90; Table 3), photogrammetry parameter set (1-12; Table 4), tree height class (> 10 m or > 20 m), and tree position class (all trees or dominant trees only). Using only those tree detection algorithms, we identified the photogrammetry parameter sets that most consistently yielded the highest, or near-highest, F scores across all factorial combinations of flight altitude, tree height class, and tree position class (Appendix S2: Table S3). We selected four photogrammetry parameter sets. Using only those four sets, we then selected the tree detection parameter sets that most consistently yielded the highest, or near-highest, F scores across different factorial combinations of photogrammetry parameter set, flight altitude, tree height class, and tree position class (Appendix S2: Table S4). We selected 8 tree detection parameter sets.

To quantify the influence of flight altitude, image overlap, and camera pitch on ITD performance (Stage 2), we used the four best-performing photogrammetry parameter sets, combined factorially with the eight best-performing tree detection methods, to produce 32 tree maps from each of the 22 different photo sets (Table 3). When plotting or describing tree detection performance achieved with any of these photo sets, we report the F score obtained from the tree detection method that produced the maximum F score for that photoset.

Evaluation of drone-based tree height measurement

To evaluate the potential to measure tree heights using drone imagery, we extracted tree heights from the canopy height model produced by using photogrammetry parameter set 16 (Table 4) on the high (120 m) nadir photo set with 90% front and side image overlap. We extracted the height value from the CHM pixel beneath each detected treetop. We then compared these extracted heights to the ground-measured heights of the ground-truth trees to which the drone-detected trees were paired (see *ITD performance evaluation*). Ground-truth trees that were not paired with drone-detected trees, and vice versa, were not included in the comparison.

Results

Stage 1: Optimal photogrammetry and tree detection parameters

Photogrammetry parameter combination 16 (medium alignment quality, high dense cloud quality, moderate depth filtering) consistently enabled the most accurate tree detection performance as quantified by F score (Fig. 2 and Appendix S2: Table S3), though the differences among parameter combinations were relatively small ($\Delta F < 0.04$). Medium alignment quality and high dense cloud quality both involve upscaling (coarsening) the image by a factor of 2 in both dimensions prior to running the algorithm. Parameter set 16 achieved the highest (or within 0.005 of the highest) F scores across all factorial combinations of flight altitude (90 m or 120 m), tree position (all trees or dominant trees), and tree height class (> 10 m or > 20 m). Therefore, for further evaluation, we focused on parameter set 16, along with parameter sets 9, 11, and 15, which were among the best-performing parameter sets for multiple combinations of tree height, tree position, and flight altitude (Appendix S2: Table S5). We thus selected a total of four photogrammetry parameter sets for further evaluation.

The most accurate tree detection methods, as quantified by F score, were all CHM-based VWF methods (Appendix S2: Table S4). This was true across all factorial combinations of flight altitude (90 m or 120 m), tree height class (> 10 m or > 20 m), tree position (all trees or dominant trees), and photogrammetry parameters (sets 9, 11, 15, and 16). Across all of these combinations, methods vwf_121 and vwf_196 most consistently achieved the highest (or within 0.005 of the highest) F scores for tree detection accuracy (Appendix S2: Table S4). Therefore, for further evaluation, we focused on these methods, along with six other consistently top-performing methods, vwf_109, vwf_110, vwf_113, vwf_120, vwf_122, vwf_185, for a total of 8 tree detection methods.

For a given scenario (e.g., flight altitude, tree position, tree height, camera pitch, and photo overlap), the F score achieved by the combination of photogrammetry parameter set 16 and tree detection method vwf_196 was generally within 0.01 of the maximum F score achieved by the optimal combination of photogrammetry parameter set (out of the four best-performing options) and tree detection method (out of the eight best-performing options) (e.g., Table 5). The difference in F score was less than 0.01 in approximately 80% of scenarios, particularly those with at least 90% front and side photo overlap and nadir images (Appendix S2: Table S5). In photo sets with less overlap and/or oblique images, other photogrammetry and tree detection parameters often performed better (F score difference > 0.01), but for these scenarios, even the optimal photogrammetry and tree detection parameter combinations yielded inferior tree mapping performance relative to higher overlap and/or nadir imagery (see next section).

For nadir photo sets with at least 90% front and side overlap, the optimal combination of photogrammetry and tree detection parameters achieved tree mapping accuracy ranging between F = 0.67 and F = 0.87 (Appendix S2: Table S5). For example, for dominant trees > 10 m tall, the optimal methods (photogrammetry parameter set 16 paired with tree detection method vwf_196) achieved an F score of 0.78, with a sensitivity of 0.69 and a precision of 0.90 (Table 5). Generally, precision was greater than sensitivity (Table 5 and Appendix S2: Table S5).

Table 5: Tree mapping accuracy achieved with the optimal combination of photogrammetry parameter set and tree detection method (Category 1) or with the specific combination of photogrammetry parameter set 16 and tree detection method vwf_196 (Category 2) for each factorial combination of tree position (dominant or all) and tree height class (> 20 m or > 10 m). All scenarios use the high (120 m altitude) nadir photo set with 90% front and side overlap. For two scenarios (dominant trees > 10 m and all trees > 20 m), the combination of photogrammetry parameter set 16 and tree detection method vwf_196 is the optimal combination. For accuracy metrics for different flight altitudes, camera pitches, and photo overlaps, see Appendix S2: Table S5.

		Category 1: Photogrammetry and tree detection parameter sets yielding maximum F					**Category 2: Photogrammetry parameter set 16 and tree detection method vwf_196**		
Canopy position	**Tree height**	**Photogrammetry parameter set**	**Tree detection method**	**F score**	**Sensitivity**	**Precision**	**F score**	**Sensitivity**	**Precision**
dominant	> 20 m	11	vwf_122	0.865	0.838	0.894	0.864	0.841	0.887
dominant	> 10 m	16	vwf_196	0.783	0.691	0.903	0.783	0.691	0.903
all	> 20 m	16	vwf_196	0.826	0.756	0.909	0.826	0.756	0.909
all	> 10 m	15	vwf_121	0.672	0.571	0.814	0.665	0.519	0.924

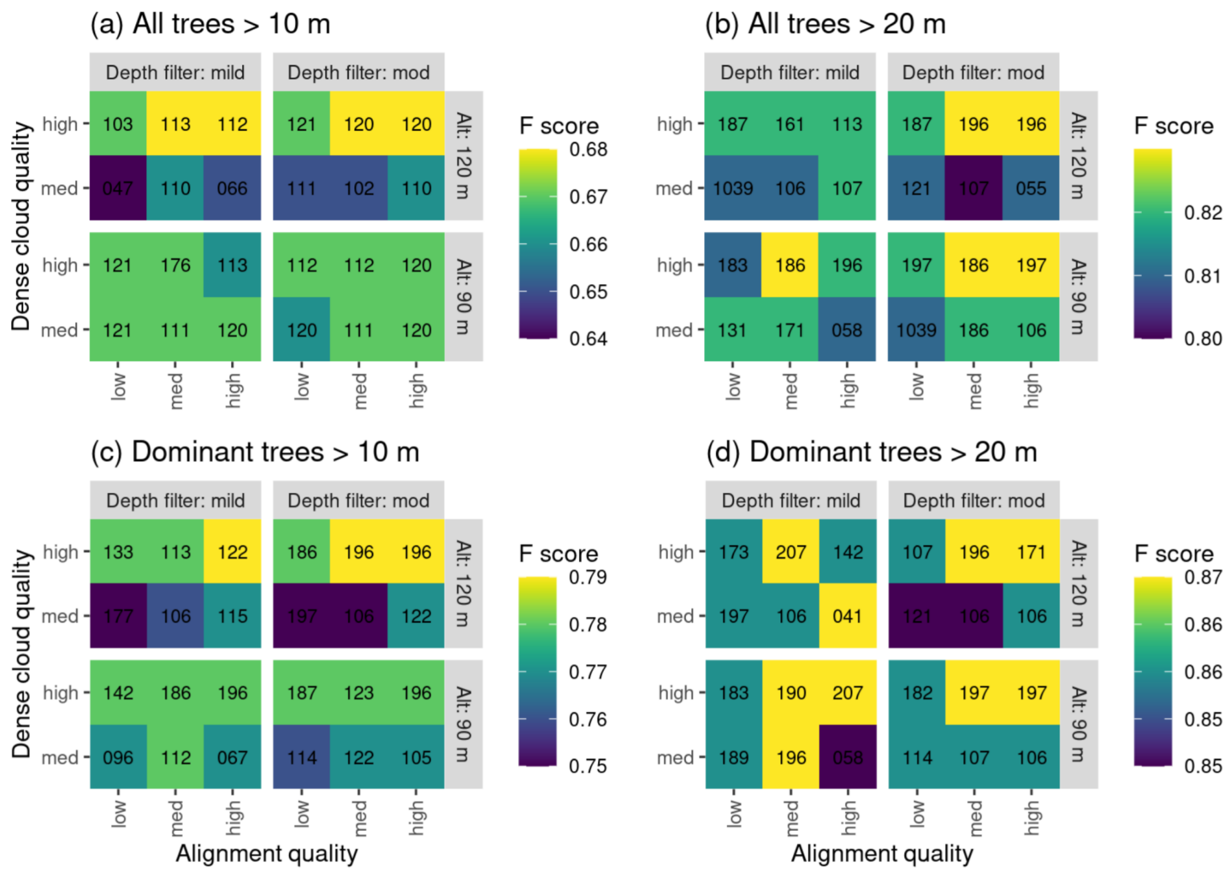

Fig. 2: Individual tree detection performance of different photogrammetry parameter combinations at two flight altitudes, for all trees (a, b) and dominant trees (c,d) with height > 10 m (a, c) or height > 20 m (b, d). The number in each cell indicates the ID of the tree detection method (Appendix S2: Table S1-S2) that yielded the maximum F score for the particular combination of parameters; 3-digit numbers refer to VWF methods, while 4-digit numbers refer to point cloud-based methods. The F score itself is indicated by the color. The aerial photo sets processed were the high nadir (Alt: 120 m) set and the low nadir (Alt: 90 m) set (both with 90% front and side image overlap) (bolded entries in Table 3).

Stage 2: Optimal image collection parameters

Tree mapping accuracy tended to increase with increasing image overlap, to a point: once overlap reached 90%/80% (front/side), additional increase in overlap (to 90%/90% or greater) yielded little increase in accuracy (Fig. 3). At 90%/90% overlap, both 120 m and 90 m nadir flights yielded F scores of about 0.78 for dominant trees > 10 m tall and about 0.86 for dominant trees > 20 m tall (Table 5). Among nadir image sets, higher-altitude (120 m) sets tended to yield greater accuracy than lower-altitude sets when image overlaps were lower (below 90%/90%) and similar accuracy when overlaps were greater (90%/90% and greater) (Fig. 3). Interestingly, even though the 90%/80% and 80%/90% overlap image sets contained roughly the same image density, the former consistently enabled substantially greater tree mapping accuracy, for both 120 m and 90 m flights (Fig. 3).

Nadir imagery tended to achieve accuracy greater than or comparable to that of oblique or nadir-oblique composite imagery. The 120 m composite nadir-oblique image set performed as well as (at 95% front and side overlap) or substantially better than (at 90% front and side overlap) the 90 m composite pitch image set. For a similar image density (i.e., number of images), a 120 m nadir flight (at, e.g., 90%/80% overlap) yielded similar accuracy as the oblique flights (at, e.g., 85%/85% nominal overlap).

All of the results discussed thus far in this section assume that a given image set is processed using the photogrammetry and tree detection parameters that yield the greatest accuracy for that set. When using a single top-performing photogrammetry parameter set (16) combined with a single top-performing tree detection method (vwf_196), the patterns remain qualitatively very similar, with generally only very small shifts in tree detection accuracy (Fig. S2).

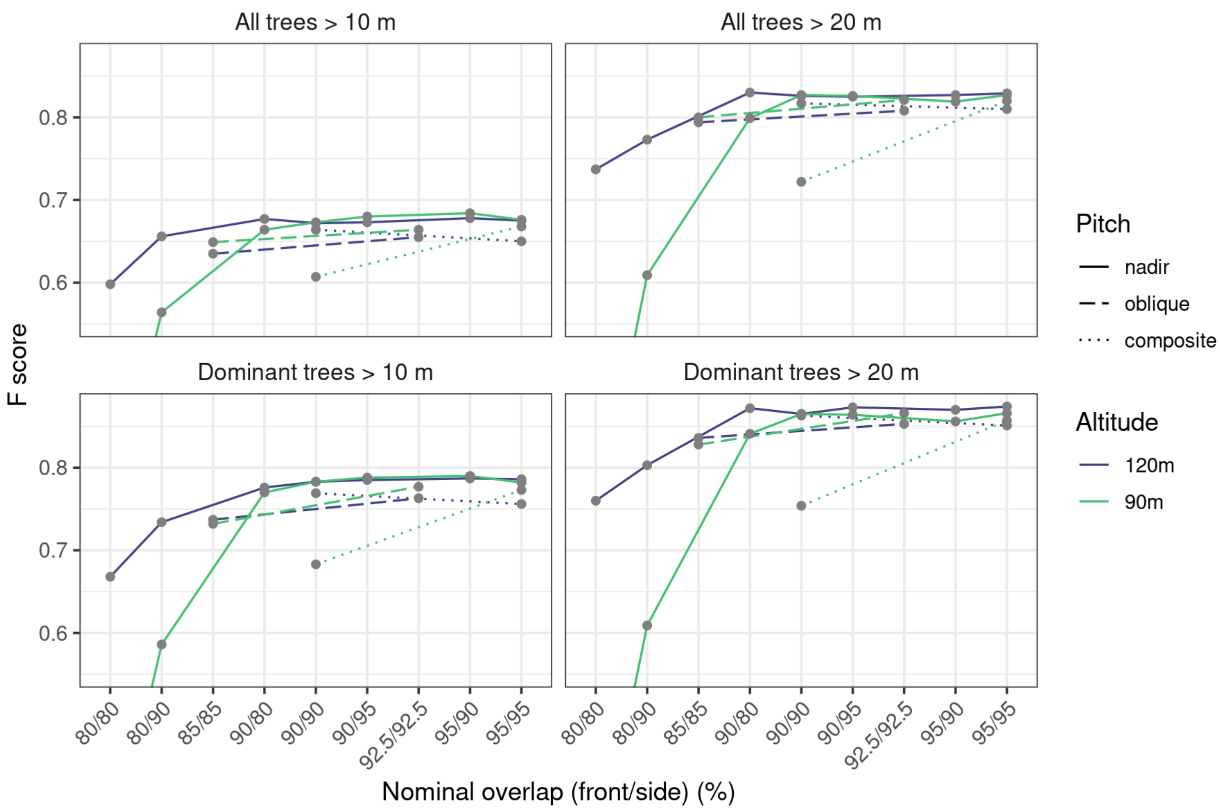

Fig. 3: Individual tree detection F score for different flight altitude, camera pitch, and image overlap combinations. For each combination, 8 top-performing tree detection methods were combined factorially with 4 top-performing photogrammetry processing parameter sets (see *Table 1: Stage 2*), and the F score depicted is the maximum across these 32 factorial combinations. For a version of this figure that uses only the single consistently best-performing tree detection method (vwf_196) combined with the best-performing photogrammetry parameter set (16), see Fig. S2.

Tree height measurement

Tree height measurement was generally highly accurate, with drone-measured and ground-measured tree heights corresponding with $R^2 = 0.95$, a mean bias of -0.86 m (with drone-derived heights generally shorter than their ground-truth counterparts), and a mean absolute error of 1.82 m (Fig. 4). The mean absolute error as a percentage of each tree's height was 9% and the mean bias was -3%.

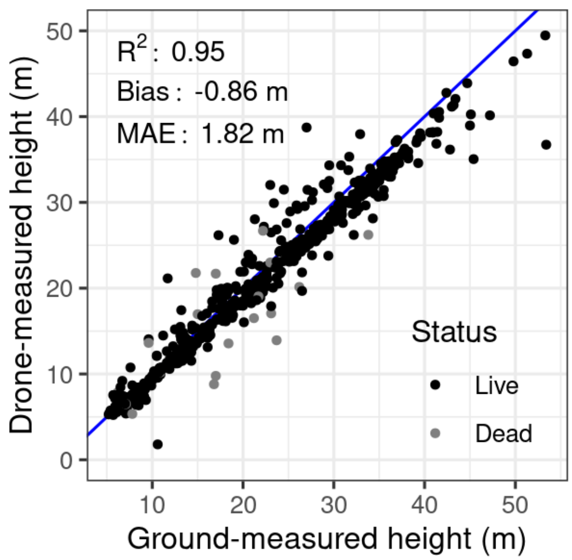

Fig. 4: Drone-based tree height measurements (height value of the CHM at each treetop location) relative to ground-truth tree heights for the most consistently best-performing tree detection method (vwf_196) applied to the CHM produced using the most consistently high-performing photogrammetry parameter combination (16) on the high (120 m) nadir 90% front and side overlap photo set.

Discussion

Imagery acquisition and processing

Our work helps to identify top-performing approaches to imagery collection and processing for SfM-based forest mapping in structurally complex conifer forests. Several clear and consistent results can help forest scientists and managers efficiently produce high-quality forest maps. First, a high (120 m) flight altitude consistently yielded tree maps with accuracy better than or effectively equivalent to those obtained from lower (90 m) flights (Fig. 3), consistent with previous observations that flight altitude has minimal impact (Swayze et al., 2021; Torres-Sánchez et al., 2018). Even in contexts where stem map quality is insensitive to flight altitude (in our case, when image overlap is 90% or greater), 120 m flights will likely be preferred given that they require fewer images to cover a landscape (as each image encompasses more ground area) and therefore less flight time.

Similarly, our work reveals little if any gain in ITD accuracy by increasing image overlap above 90% (front and side) (Fig. 3), consistent with previous results showing decreasing marginal returns to ITD accuracy with increasingly high overlap (Torres-Sánchez et al., 2018). In fact, given that increasing image overlap can substantially increase flight time (e.g., increasing side overlap from 90% to 95% doubles the number of transects, thus doubling flight time), flights with overlap > 90% may be undesirable. Reducing side overlap to 80% (while keeping front overlap at 90%) resulted in only minimal change in ITD accuracy. Therefore, given flight time constraints or the need to cover extensive area, 90%/80% front/side overlap may be preferable. Surprisingly, photo sets with 90%/80% front/side overlap consistently yielded ITD accuracy substantially greater than that from sets with 80%/90% front/side overlap (Fig. 3), despite the fact that the image density of these two sets is nominally identical.

Our tests of camera pitch revealed that oblique (25°) and oblique-nadir composite imagery, regardless of flight altitude, yielded ITD accuracy worse than nadir imagery collected at 120 m. This finding is surprising because oblique imagery is known to yield more accurate terrain models (Nesbit & Hugenholtz, 2019) and increase understory point cloud density (Díaz et al., 2020), but it corroborates existing evidence that for ITD specifically, greater accuracy is achieved with nadir imagery (Swayze et al., 2021). Although the improved understory imaging that is achieved by using oblique imagery can improve estimates of tree DBH (by enabling more accurate 3D modeling of tree stems; Swayze et al., 2021), it apparently does not improve the potential for detection of understory trees. This limitation to improvement may be explained by the fact that all CHM-based tree detection algorithms and many point cloud-based tree detection algorithms (e.g., Li et al., 2012) are not designed to detect one tree beneath another, so improved imaging of the understory cannot translate to improved tree detection. Improvements to multi-layer tree detection algorithms (e.g., Torresan et al., 2020; Xiao et al., 2019), and implementations of them in common point cloud processing platforms (e.g., the R package lidR; Roussel, 2021a), may make understory imaging (and thus oblique camera angles) more valuable for ITD in the future.

We expect our results are applicable to many widely used, relatively low cost drones with camera resolution and field of view similar to ours. In fact, given that all image processing steps in the optimal parameterization utilize images that have been upscaled (coarsened) 2-fold in both dimensions (thus converting a 20 megapixel image to 5 megapixels), the same dataset could in theory be generated with a 5 megapixel camera by eliminating the upscaling step. Similarly, imagery from a higher-resolution camera could be used optimally by increasing the upscaling factor. While this may represent a waste of data, the coarser scale may actually achieve greater mapping accuracy given that tree canopies largely consist of small surfaces (e.g., leaves, branches) that are susceptible to moving in the wind and thus confounding the image-matching algorithms central to the photogrammetry software.

Tree detection algorithms

Despite testing 6 point cloud-based ITD algorithms (and 58 different parameterizations of them), the CHM-based VWF algorithm consistently performed the best (Appendix S2: Table S4), potentially a consequence of the fact that the point cloud based-methods we tested are not designed to detect one tree beneath another and therefore provide little additional fidelity relative to a CHM (see Discussion section *Imagery acquisition and processing*).

As with other SfM-based work (e.g., Creasy et al., 2021; Tinkham & Swayze, 2021) and LiDAR-based work (Ferraz et al., 2012; Jeronimo et al., 2018), we observed substantially improved ITD performance for taller trees and canopy-dominant trees vs. all trees (e.g., F = 0.78 for canopy-dominant trees > 10 m height vs. F = 0.67 for all trees > 10 m height). This pattern makes sense considering structure can only be mapped for surfaces that are detected by the sensor (which are disproportionately the top-of-canopy objects, especially for SfM; Jayathunga et al., 2018; Lisein et al., 2013). Even when using LiDAR, which usually can penetrate the canopy to some extent, understory and mid-story detail, and thus potential to detect trees there, is limited (Richardson & Moskal, 2011) and has led some to re-focus detection and mapping of individual trees (ITD) toward detection and mapping of tree-approximate objects (TAOs), which can include single trees and clusters of trees that are not differentiable (Jeronimo et al., 2018; North et al., 2017). Maps of the size and arrangement of TAOs may be valuable for some management applications (Jeronimo et al., 2018; North et al., 2017), and important ecological questions can be addressed using maps of the specific trees visible from above (Brandt et al., 2020; Weinstein et al., 2021) or detectable using SfM that is not canopy-penetrating (Koontz et al., 2021). Our calculation of ITD accuracy metrics specifically for "overstory" trees helps to provide a sense of TAO mapping accuracy. Given that we used a conservative set of parameters for classifying a tree as "canopy dominant" (Fig. S1), our accuracy metrics may be underestimates.

Notably, our ITD precision values were consistently higher than the sensitivity values, especially for all trees (as opposed to canopy-dominant trees) (Table 5 and Appendix S2: Table S5), indicating that the ITD algorithm failed to detect some trees at the expense of minimizing false-positives. This suggests that there is some potential to select an ITD parameterization with greater tree detection sensitivity. This may increase the false-positive rate (resulting in an overall lower F score), but future work may incorporate an additional "detected tree screening" stage that uses information besides the CHM or point cloud to identify and reject false positives. For example, Bonnet et al. (2017) used a machine learning approach to predict tree detections as true or false positives based on the textural and spectral characteristics of the detected objects and thereby reduced the false-positive rate from 75-82% to 3-8%. Incorporating both structural and spectral data (e.g., taking advantage of the fact that points in SfM-derived point clouds, in contrast to LiDAR-derived clouds, can be assigned spectral values) in tree detection algorithms may improve tree detection sensitivity (Yancho et al., 2019).

Tree height measurement and matching of ground and drone trees

The canopy height model resulting from the optimal photogrammetry parameter set provided a relatively accurate representation of tree heights (Fig. 4). The small negative height bias (CHM heights < field-measured heights) generally increased with increasing tree height, suggesting either (a) disproportionate overestimation of tall tree heights during ground surveys or (b) disproportionate underestimation of tall tree heights by the photogrammetry algorithm. Given that CHM generation involves some degree of interpolation and smoothing of the point cloud, it may make sense that objects that are disproportionately tall relative to their surroundings are underestimated by the CHM. Nonetheless, the mean absolute height error was relatively small (1.8 m or 9% of tree height). Further, given that our algorithm for matching SfM-detected trees with ground-measured trees required the SfM tree to be within ± 50% of the height of the ground tree, the fact that the mean height difference was only 9% strongly suggests that trees were generally matched correctly. Our SfM-based tree height measurement accuracy was generally comparable to or better than other SfM-based approaches, which have obtained R^2 = 0.71 (Belmonte et al., 2020), RMSE = 9-15% (Creasy et al., 2021), RMSE = 24% (Tinkham & Swayze, 2021), and R^2 = 0.99 and RMSE = 18% (Swayze et al., 2021).

ITD performance assessment and conclusions

Potentially due to the comprehensive evaluation of numerous SfM imagery collection, imagery processing, and tree detection methods, the ITD performance we achieved meets or exceeds expectations based on previous work. With relatively high image overlap (> 90% front and side), Swayze et al. (2021) obtained a maximum F score of 0.77 for all trees, and Tinkham and Swayze (2021) obtained a maximum F score of 0.72 for overstory trees. The work by Tinkham and Swayze (2021) and Swayze et al. (2021) was conducted in a relatively low-density forest (trees > 5 m height: 374 ha^{-1} relative to our 551 ha^{-1}) with low structural complexity (generally two distinct size classes that are spatially clustered rather than interspersed with layered strata) and a single dominant conifer species, so the F scores we obtained (0.67-0.86 depending on canopy position and height; Table 5) suggest strong performance. The ITD performance we achieved appears improved relative to that observed by Koontz et al. (2021) in Sierra Nevada forests of similar or lower density, where RMSE of tree count ranged between 46% and 75% of ground-mapped tree count. Our understory (F score: 0.67) and overstory (F score: 0.78-0.87) ITD accuracy was also greater than that obtained by Creasy et al. (2021) (F score: 0.51-0.57 for understory and intermediate trees and F score: 0.75 for overstory trees). The stands studied by Creasy et al. (2021) had much greater reported density (1379-1537 trees ha^{-1} for trees > 6-8 m height), though these reported density values may be overestimated given the forest type (nearly monodominant ponderosa pine) and given that a different study at one of the same sites (Swayze et al. 2021) reported density of trees > 5 m height to be 374 trees ha^{-1}. In an Arizona ponderosa pine forest, Belmonte et al. (2020) detected trees in low-density stands (mean density: 59 trees ha^{-1}) with F = 0.94, in moderate-density stands (mean density: 139 trees ha^{-1}) with F = 0.8, and in high-density stands (mean density: 778 trees ha^{-1}) with F = 0.44.

The majority of SfM-based ITD work to date has been conducted in relatively low density monodominant stands with low structural complexity. Our work demonstrates that SfM-based ITD can also be a practical approach to tree mapping in denser, more structurally complex stands, especially if the focus is on canopy-dominant trees or TAOs. To evaluate the extent to which the ITD accuracy and optimal parameter sets we identified may extend to other forest stands, perhaps the most important considerations are stand density and structural complexity (Jeronimo et al., 2018). In forests with lower tree density and limited multi-stratum structure, such as many ponderosa pine-dominated forests of the southwestern U.S. (e.g., Swayze et al. 2021), we might expect higher accuracy than we achieved; we might expect the reverse for denser or more structurally complex stands. Historical densities of trees > 10 cm DBH in the yellow pine and mixed-conifer forests of California's Sierra Nevada averaged roughly 195 trees ha^{-1} (Safford & Stevens, 2017; Young et al., 2020), relative to the 593 trees ha^{-1} in our mixed-conifer stand. With contemporary stands roughly 2-4-fold denser than the historical average (Safford & Stevens, 2017) (therefore, roughly 400-800 trees ha^{-1}), our focal stand may be roughly reflective of mean contemporary California mixed-conifer forest structure and thus of expected ITD performance. In denser stands with strong multi-stratum structure, the use of oblique images, coupled with a point-cloud based ITD algorithm, will likely become more important for capturing understory trees (see Discussion section *Imagery acquisition*). With additional refinements (e.g., use of a more sensitive tree detection algorithm with a false-positive filtering step, improvement of point cloud-based multi-layer tree detection algorithms, and application of deep learning computer vision to tree detection; Weinstein et al., 2020, 2021), the accuracy and applicability of drone-based forest mapping will continue to improve.

Acknowledgments

Our Emerald Point study site is part of the ancestral lands of the Washoe people. We thank data technicians H. de la Calle and S. Sundaram for their careful organization of the drone imagery, identification of ground control points, and preparation of the ground-truth stem map data. We thank A. Barker and R. Cuevas for assisting with ground-truth stem map data collection and D. Shaw for facilitating field logistics. We thank A. Latimer for assistance acquiring drone equipment and computing resources. We thank A. Mandel and other contributors to the reproducible photogrammetry workflow software library we used. Funding for this project was provided by the California Department of Forestry and Fire Protection's Forest Health Program as part of the California Climate Investments Program.

Author contributions: DJNY and MJK conceived the ideas and designed the methodology; DJNY and JW collected the data; DJNY analysed the data; DJNY led the writing of the manuscript. All authors contributed critically to the drafts and gave final approval for publication.

Data availability: The raw and processed data and code supporting this publication are available via the Open Science Framework (https://osf.io/kb3nj/; DOI: 10.17605/OSF.IO/KB3NJ; Young et al., 2021).

Literature cited

Agisoft. (2020). *Metashape v1.6 downscale parameter*. https://www.agisoft.com/forum/index.php?topic=11697.0

Belmonte, A., Sankey, T., Biederman, J. A., Bradford, J., Goetz, S. J., Kolb, T., & Woolley, T. (2020). UAV-derived estimates of forest structure to inform ponderosa pine forest restoration. *Remote Sensing in Ecology and Conservation*, *6*(2), 181–197. https://doi.org/10.1002/rse2.137

Bonnet, S., Lisein, J., & Lejeune, P. (2017). Comparison of UAS photogrammetric products for tree detection and characterization of coniferous stands. *International Journal of Remote Sensing*, *38*(19), 5310–5337. https://doi.org/10.1080/01431161.2017.1338839

Brandt, M., Tucker, C. J., Kariryaa, A., Rasmussen, K., Abel, C., Small, J., Chave, J., Rasmussen, L. V., Hiernaux, P., Diouf, A. A., Kergoat, L., Mertz, O., Igel, C., Gieseke, F., Schöning, J., Li, S., Melocik, K., Meyer, J., Sinno, S., … Fensholt, R. (2020). An unexpectedly large count of trees in the West African Sahara and Sahel. *Nature*, 1–5. https://doi.org/10.1038/s41586-020-2824-5

Camarretta, N., Harrison, P. A., Bailey, T., Potts, B., Lucieer, A., Davidson, N., & Hunt, M. (2020). Monitoring forest structure to guide adaptive management of forest restoration: A review of remote sensing approaches. *New Forests*, *51*(4), 573–596. https://doi.org/10.1007/s11056-019-09754-5

Creasy, M. B., Tinkham, W. T., Hoffman, C. M., & Vogeler, J. C. (2021). Potential for Individual Tree Monitoring in Ponderosa Pine-Dominated Forests Using Unmanned Aerial System Structure from Motion Point Clouds. *Canadian Journal of Forest Research*, cjfr-2020-0433. https://doi.org/10.1139/cjfr-2020-0433

Dandois, J. P., & Ellis, E. C. (2013). High spatial resolution three-dimensional mapping of vegetation spectral dynamics using computer vision. *Remote Sensing of Environment*, *136*, 259–276. https://doi.org/10.1016/j.rse.2013.04.005

Dandois, J. P., Olano, M., & Ellis, E. C. (2015). Optimal Altitude, Overlap, and Weather Conditions for Computer Vision UAV Estimates of Forest Structure. *Remote Sensing*, *7*(10), 13895–13920. https://doi.org/10.3390/rs71013895

De Luca, G., N. Silva, J. M., Cerasoli, S., Araújo, J., Campos, J., Di Fazio, S., & Modica, G. (2019). Object-Based Land Cover Classification of Cork Oak Woodlands using UAV Imagery and Orfeo ToolBox. *Remote Sensing*, *11*(10), 1238. https://doi.org/10.3390/rs11101238

Díaz, G. M., Mohr-Bell, D., Garrett, M., Muñoz, L., & Lencinas, J. D. (2020). Customizing unmanned aircraft systems to reduce forest inventory costs: Can oblique images substantially improve the 3D reconstruction of the canopy? *International Journal of Remote Sensing*, *41*(9), 3480–3510. https://doi.org/10.1080/01431161.2019.1706200

Farr, T. G., Rosen, P. A., Caro, E., Crippen, R., Duren, R., Hensley, S., Kobrick, M., Paller, M., Rodriguez, E., Roth, L., Seal, D., Shaffer, S., Shimada, J., Umland, J., Werner, M., Oskin, M., Burbank, D., & Alsdorf, D. (2007). The Shuttle Radar Topography Mission. *Reviews of Geophysics*, *45*(2). https://doi.org/10.1029/2005RG000183

Ferraz, A., Bretar, F., Jacquemoud, S., Gonçalves, G., Pereira, L., Tomé, M., & Soares, P. (2012). 3-D mapping of a multi-layered Mediterranean forest using ALS data. *Remote*

Sensing of Environment, *121*, 210–223. https://doi.org/10.1016/j.rse.2012.01.020
Frey, J., Kovach, K., Stemmler, S., & Koch, B. (2018). UAV Photogrammetry of Forests as a Vulnerable Process. A Sensitivity Analysis for a Structure from Motion RGB-Image Pipeline. *Remote Sensing*, *10*(6), 912. https://doi.org/10.3390/rs10060912
Gray, A. N., Brandeis, T. J., Shaw, J. D., McWilliams, W. H., & Miles, P. (2012). Forest Inventory and Analysis Database of the United States of America (FIA). *In: Dengler, J.; Oldeland, J.; Jansen, F.; Chytry, M.; Ewald, J., Finckh, M.; Glockler, F.; Lopez-Gonzalez, G.; Peet, R. K.; Schaminee, J .H. J., Eds. Vegetation Databases for the 21st Century. Biodiversity and Ecology. 4: 225-231.*, 225–231. https://doi.org/10.7809/b-e.00079
Hubbell, S. P., Foster, R. B., O'Brien, S. T., Harms, K. E., Condit, R., Wechsler, B., Wright, S. J., & Lao, S. L. de. (1999). Light-Gap Disturbances, Recruitment Limitation, and Tree Diversity in a Neotropical Forest. *Science*, *283*(5401), 554–557. https://doi.org/10.1126/science.283.5401.554
Jayathunga, S., Owari, T., & Tsuyuki, S. (2018). The use of fixed–wing UAV photogrammetry with LiDAR DTM to estimate merchantable volume and carbon stock in living biomass over a mixed conifer–broadleaf forest. *International Journal of Applied Earth Observation and Geoinformation*, *73*, 767–777. https://doi.org/10.1016/j.jag.2018.08.017
Jeronimo, S. M. A., Kane, V. R., Churchill, D. J., McGaughey, R. J., & Franklin, J. F. (2018). Applying LiDAR Individual Tree Detection to Management of Structurally Diverse Forest Landscapes. *Journal of Forestry*, *116*(4), 336–346. https://doi.org/10.1093/jofore/fvy023
Koontz, M. J., Latimer, A. M., Mortenson, L. A., Fettig, C. J., & North, M. P. (2021). Cross-scale interaction of host tree size and climatic water deficit governs bark beetle-induced tree mortality. *Nature Communications*, *12*(1), 129. https://doi.org/10.1038/s41467-020-20455-y
Lasky, J. R., Uriarte, M., Boukili, V. K., Erickson, D. L., Kress, W. J., & Chazdon, R. L. (2014). The relationship between tree biodiversity and biomass dynamics changes with tropical forest succession. *Ecology Letters*, *17*(9), 1158–1167. https://doi.org/10.1111/ele.12322
Li, W., Guo, Q., Jakubowski, M. K., & Kelly, M. (2012). A New Method for Segmenting Individual Trees from the Lidar Point Cloud. *Photogrammetric Engineering & Remote Sensing*, *78*(1), 75–84. https://doi.org/10.14358/PERS.78.1.75
Lisein, J., Pierrot-Deseilligny, M., Bonnet, S., & Lejeune, P. (2013). A Photogrammetric Workflow for the Creation of a Forest Canopy Height Model from Small Unmanned Aerial System Imagery. *Forests*, *4*(4), 922–944. https://doi.org/10.3390/f4040922
Mlambo, R., Woodhouse, I. H., Gerard, F., & Anderson, K. (2017). Structure from Motion (SfM) Photogrammetry with Drone Data: A Low Cost Method for Monitoring Greenhouse Gas Emissions from Forests in Developing Countries. *Forests*, *8*(3), 68. https://doi.org/10.3390/f8030068
Mohan, M., Silva, C., Klauberg, C., Jat, P., Catts, G., Cardil, A., Hudak, A., & Dia, M. (2017). Individual tree detection from unmanned aerial vehicle (UAV) derived canopy height model in an open canopy mixed conifer forest. *Forests*, *8*(9), 340. https://doi.org/10.3390/f8090340
Nesbit, P. R., & Hugenholtz, C. H. (2019). Enhancing UAV–SfM 3D Model Accuracy in High-Relief Landscapes by Incorporating Oblique Images. *Remote Sensing*, *11*(3), 239. https://doi.org/10.3390/rs11030239

Ni, W., Sun, G., Pang, Y., Zhang, Z., Liu, J., Yang, A., Wang, Y., & Zhang, D. (2018). Mapping Three-Dimensional Structures of Forest Canopy Using UAV Stereo Imagery: Evaluating Impacts of Forward Overlaps and Image Resolutions With LiDAR Data as Reference. *IEEE Journal of Selected Topics in Applied Earth Observations and Remote Sensing*, *11*(10), 3578–3589. https://doi.org/10.1109/JSTARS.2018.2867945

North, M. P., Kane, J. T., Kane, V. R., Asner, G. P., Berigan, W., Churchill, D. J., Conway, S., Gutiérrez, R. J., Jeronimo, S., Keane, J., Koltunov, A., Mark, T., Moskal, M., Munton, T., Peery, Z., Ramirez, C., Sollmann, R., White, A., & Whitmore, S. (2017). Cover of tall trees best predicts California spotted owl habitat. *Forest Ecology and Management*, *405*, 166–178. https://doi.org/10.1016/j.foreco.2017.09.019

North, M. P., York, R. A., Collins, B. M., Hurteau, M. D., Jones, G. M., Knapp, E. E., Kobziar, L., McCann, H., Meyer, M. D., Stephens, S. L., Tompkins, R. E., & Tubbesing, C. L. (2021). Pyrosilviculture Needed for Landscape Resilience of Dry Western United States Forests. *Journal of Forestry*, *119*(5), 520–544. https://doi.org/10.1093/jofore/fvab026

Over, J.-S. R., Ritchie, A. C., Kranenburg, C. J., Brown, J. A., Buscombe, D. D., Noble, T., Sherwood, C. R., Warrick, J. A., & Wernette, P. A. (2021). Processing coastal imagery with Agisoft Metashape Professional Edition, version 1.6—Structure from motion workflow documentation. In *Processing coastal imagery with Agisoft Metashape Professional Edition, version 1.6—Structure from motion workflow documentation* (USGS Numbered Series No. 2021–1039; Open-File Report, Vols. 2021–1039, p. 46). U.S. Geological Survey. https://doi.org/10.3133/ofr20211039

Plowright, A. (2021). *ForestTools: Analyzing Remotely Sensed Forest Data*. Comprehensive R Archive Network (CRAN). https://CRAN.R-project.org/package=ForestTools

Popescu, S. C., & Wynne, R. H. (2004). Seeing the Trees in the Forest. *Photogrammetric Engineering & Remote Sensing*, *70*(5), 589–604. https://doi.org/10.14358/PERS.70.5.589

Puliti, S., Solberg, S., & Granhus, A. (2019). Use of UAV photogrammetric data for estimation of biophysical properties in forest stands under regeneration. *Remote Sensing*, *11*(3), 233. https://doi.org/10.3390/rs11030233

Richardson, J. J., & Moskal, L. M. (2011). Strengths and limitations of assessing forest density and spatial configuration with aerial LiDAR. *Remote Sensing of Environment*, *115*(10), 2640–2651. https://doi.org/10.1016/j.rse.2011.05.020

Rodman, K. C., Veblen, T. T., Saraceni, S., & Chapman, T. B. (2019). Wildfire activity and land use drove 20th-century changes in forest cover in the Colorado front range. *Ecosphere*, *10*(2), e02594. https://doi.org/10.1002/ecs2.2594

Roussel, J.-R. (2021a, May 20). *Airborne LiDAR Data Manipulation and Visualization for Forestry Applications [R package lidR version 3.0.4]*. Comprehensive R Archive Network (CRAN). https://CRAN.R-project.org/package=lidR

Roussel, J.-R. (2021b, May 20). *Extra functions and algorithms for lidR package [R package lidRplugins version 0.2.0]*. https://github.com/Jean-Romain/lidRplugins

Safford, H. D., & Stevens, J. T. (2017). Natural range of variation for yellow pine and mixed-conifer forests in the Sierra Nevada, southern Cascades, and Modoc and Inyo National Forests, California, USA. *Gen. Tech. Rep. PSW-GTR-256. Albany, CA: U.S. Department of Agriculture, Forest Service, Pacific Southwest Research Station. 229 p.*,

256. https://www.fs.usda.gov/treesearch/pubs/55393
Shin, P., Sankey, T., Moore, M. M., & Thode, A. E. (2018). Evaluating Unmanned Aerial Vehicle Images for Estimating Forest Canopy Fuels in a Ponderosa Pine Stand. *Remote Sensing*, *10*(8), 1266. https://doi.org/10.3390/rs10081266
Silva, C. A., Hudak, A. T., Vierling, L. A., Loudermilk, E. L., O'Brien, J. J., Hiers, J. K., Jack, S. B., Gonzalez-Benecke, C., Lee, H., Falkowski, M. J., & Khosravipour, A. (2016). Imputation of Individual Longleaf Pine (Pinus palustris Mill.) Tree Attributes from Field and LiDAR Data. *Canadian Journal of Remote Sensing*, *42*(5), 554–573. https://doi.org/10.1080/07038992.2016.1196582
Swayze, N. C., Tinkham, W. T., Vogeler, J. C., & Hudak, A. T. (2021). Influence of flight parameters on UAS-based monitoring of tree height, diameter, and density. *Remote Sensing of Environment*, *263*, 112540. https://doi.org/10.1016/j.rse.2021.112540
Tinkham, W. T., & Swayze, N. C. (2021). Influence of Agisoft Metashape Parameters on UAS Structure from Motion Individual Tree Detection from Canopy Height Models. *Forests*, *12*(2), 250. https://doi.org/10.3390/f12020250
Torresan, C., Carotenuto, F., Chiavetta, U., Miglietta, F., Zaldei, A., & Gioli, B. (2020). Individual Tree Crown Segmentation in Two-Layered Dense Mixed Forests from UAV LiDAR Data. *Drones*, *4*(2), 10. https://doi.org/10.3390/drones4020010
Torres-Sánchez, J., López-Granados, F., Borra-Serrano, I., & Peña, J. M. (2018). Assessing UAV-collected image overlap influence on computation time and digital surface model accuracy in olive orchards. *Precision Agriculture*, *19*(1), 115–133. https://doi.org/10.1007/s11119-017-9502-0
USDA Forest Service. (2016). *Forest Inventory and Analysis Strategic Plan FS-1079*. https://www.fia.fs.fed.us/library/bus-org-documents/docs/strategic-plan-docs/FIA%20Strategic%20Plan%20FS-1079.pdf
USGS. (2017). *Unmanned Aircraft Systems Data Post-Processing: Structure-from-Motion Photogrammetry*. National Unmanned Aircraft Systems (UAS) Project Office. https://uas.usgs.gov/nupo/pdf/PhotoScanProcessingDSLRMar2017.pdf
USGS. (2018). *3DEP products and services: The National Map, 3D Elevation Program, https://nationalmap.gov/3DEP/*.
Weinstein, B. G., Marconi, S., Bohlman, S. A., Zare, A., Singh, A., Graves, S. J., & White, E. P. (2021). A remote sensing derived data set of 100 million individual tree crowns for the National Ecological Observatory Network. *ELife*, *10*, e62922. https://doi.org/10.7554/eLife.62922
Weinstein, B. G., Marconi, S., Bohlman, S. A., Zare, A., & White, E. P. (2020). Cross-site learning in deep learning RGB tree crown detection. *Ecological Informatics*, *56*, 101061. https://doi.org/10.1016/j.ecoinf.2020.101061
Westoby, M. J., Brasington, J., Glasser, N. F., Hambrey, M. J., & Reynolds, J. M. (2012). 'Structure-from-Motion' photogrammetry: A low-cost, effective tool for geoscience applications. *Geomorphology*, *179*, 300–314. https://doi.org/10.1016/j.geomorph.2012.08.021
Whittaker, R. H. (1956). Vegetation of the Great Smoky Mountains. *Ecological Monographs*, *26*(1), 1–80. https://doi.org/10.2307/1943577
Wright, S. J., Kitajima, K., Kraft, N. J. B., Reich, P. B., Wright, I. J., Bunker, D. E., Condit, R.,

Dalling, J. W., Davies, S. J., Díaz, S., Engelbrecht, B. M. J., Harms, K. E., Hubbell, S. P., Marks, C. O., Ruiz-Jaen, M. C., Salvador, C. M., & Zanne, A. E. (2010). Functional traits and the growth–mortality trade-off in tropical trees. *Ecology*, *91*(12), 3664–3674. https://doi.org/10.1890/09-2335.1

Xiao, W., Zaforemska, A., Smigaj, M., Wang, Y., & Gaulton, R. (2019). Mean Shift Segmentation Assessment for Individual Forest Tree Delineation from Airborne Lidar Data. *Remote Sensing*, *11*(11), 1263. https://doi.org/10.3390/rs11111263

Yancho, J. M. M., Coops, N. C., Tompalski, P., Goodbody, T. R. H., & Plowright, A. (2019). Fine-Scale Spatial and Spectral Clustering of UAV-Acquired Digital Aerial Photogrammetric (DAP) Point Clouds for Individual Tree Crown Detection and Segmentation. *IEEE Journal of Selected Topics in Applied Earth Observations and Remote Sensing*, *12*(10), 4131–4148. https://doi.org/10.1109/JSTARS.2019.2942811

Young, D., Alex, Alexander, MallikaNocco, & Hereñú, D. (2021). *ucdavis/metashape: V0.1.0*. Zenodo. https://doi.org/10.5281/zenodo.5088962

Young, D. J. N., Koontz, M. J., & Weeks, J. (2021). *Open Science Framework repository: Optimizing aerial imagery collection and processing parameters for drone-based individual tree mapping in structurally complex conifer forests*. https://doi.org/10.17605/OSF.IO/KB3NJ

Young, D., Meyer, M., Estes, B., Gross, S., Wuenschel, A., Restaino, C., & Safford, H. D. (2020). Forest recovery following extreme drought in California, USA: Natural patterns and effects of pre-drought management. *Ecological Applications*, *30*(1), e02002. https://doi.org/10.1002/eap.2002

Zaforemska, A., Xiao, W., & Gaulton, R. (2019). INDIVIDUAL TREE DETECTION FROM UAV LIDAR DATA IN A MIXED SPECIES WOODLAND. *ISPRS - International Archives of the Photogrammetry, Remote Sensing and Spatial Information Sciences*, *XLII-2/W13*, 657–663. https://doi.org/10.5194/isprs-archives-XLII-2-W13-657-2019